Journal of Alloys and Compounds 785 (2019) 320–327

Contents lists available at ScienceDirect

Journal of Alloys and Compounds

journal homepage: http://www.elsevier.com/locate/jalcom

Experimental investigation and phase diagram of CoCrMnNi–Fe system bridging high-entropy alloys and high-alloyed steels

Ibrahim Ondicho [a], Minku Choi [a, 1], Won-Mi Choi [b], Jong Bae Jeon [c], Hamid Reza Jafarian [d], Byeong-Joo Lee [b, **], Sun Ig Hong [e, ***], Nokeun Park [a, *]

[a] School of Materials Science and Engineering, Yeungnam University, Gyeongsan 38541, Republic of Korea
[b] Department of Materials Science and Engineering, Pohang University of Science and Technology (POSTECH), Pohang 37673, Republic of Korea
[c] Functional Components and Materials R&D Group, Korea Institute of Industrial Technology, Busan 46742, Republic of Korea
[d] School of Metallurgy and Materials Engineering, Iran University of Science and Technology, Tehran, Iran
[e] Department of Materials Science and Engineering, Chungnam National University, Daejeon 34134, Republic of Korea

ARTICLE INFO

Article history:
Received 31 October 2018
Received in revised form
3 January 2019
Accepted 11 January 2019
Available online 14 January 2019

Keywords:
Entropy
Enthalpy
Mechanical properties
Phase diagram
Microstructure
Thermodynamic modeling

ABSTRACT

An investigation of equiatomic and non-equiatomic high-entropy alloys (HEAs) and medium-entropy alloys (MEAs) was carried out by performing both thermodynamic calculations and experiments. The design strategy of the alloys was based on a constant valence electron concentration (VEC) of 8 while varying the content of Fe in a $Fe_x(CoCrMnNi)_{100-x}$ where $x = 00$, 20, 40, and 60. The X-ray diffraction results showed that the alloys have a single face-centered cubic structure at 900 °C. The tensile test results revealed that both the yield strength and ultimate tensile strength decrease as the amount of Fe is increased but the uniform elongation increases. Additionally, the strain-hardening rate is significantly enhanced at higher Fe concentrations due to the activation of deformation twinning as an additional deformation mechanism. Interestingly, the critical twinning stress is significantly reduced as the Fe content is increased from Fe00 to Fe60. As a result, the deformation twins were easily activated in a specimen deformed up to a true strain of 20% for Fe60, unlike the other alloys, which exhibited no deformation twinning at the same true strain. Furthermore, it was revealed that the frequency of deformation twinning increases proportionally with increase in the Fe content.

1. Introduction

High-entropy alloys (HEAs) constitute a unique class of alloys that has attracted significant attention from material scientists. It has been reported that their high-configurational entropy favors the formation of solid solution phases such as face-centered cubic (fcc), body-centered cubic (bcc), and hexagonal closed-packed (hcp) crystal structures against the expected intermetallic phases according to existing physical metallurgy principles [1–6] Furthermore, to maximize the mixing entropy, HEAs should contain five or more principal elements at an equiatomic or near-equiatomic percentage, with a concentration range of 5–35 at.% [1]. This distinctive alloy-design strategy is different from the traditional method of designing alloys wherein one principal element, such as Fe or Ti, is used with the addition of several other alloying elements in small amounts to improve the physical properties [7,8]. Based on this design criterion, HEAs have been reported to exhibit excellent physical properties under cryogenic, room temperature, and high-temperature conditions [3,6,9,10].

A HEA which has been the subject of considerable study is the equiatomic CoCrFeMnNi alloy commonly known as the 'Cantor alloy,' given that it was first reported by Cantor et al. [4]. This alloy has been reported to have a single fcc phase structure upon solidification and when annealed at temperatures >800 °C, although recent studies have reported that it develops intermetallic phases, such as a sigma (σ) phase, when annealed at temperatures <800 °C [4,11–13]. Researchers have reported on the numerous outstanding properties of a CoCrFeMnNi alloy relative to conventional alloys [14–16]. Otto et al. [14] observed the impressive work-hardening rate of CoCrFeMnNi alloy under cryogenic conditions. This

* Corresponding author.
** Corresponding author.
*** Corresponding author.
E-mail addresses: onsomu32@gmail.com (I. Ondicho), calphad@postech.ac.kr (B.-J. Lee), sihong@cnu.ac.kr (S.I. Hong), nokeun_park@yu.ac.kr (N. Park).
[1] Present address: Pohang Institute of Metal Industry Advancement, Pohang, Gyeongbuk 37666 Republic of Korea.

https://doi.org/10.1016/j.jallcom.2019.01.134
0925-8388/

phenomenon was attributed to the nanoscale mechanical twinning that enhances the ductility of this alloy by postponing the onset of plastic instability. Furthermore, Liu et al. [15] demonstrated that a CoCrFeMnNi alloy conforms to the classical Hall-Petch relationship, but its hardening coefficient is higher than that of a conventional alloy. On the other hand, the high-temperature characterization of this alloy system showed desirable creep resistance properties over the testing temperature range of 600–800 °C, providing an alternative for high-temperature industrial applications [16]. Further studies revealed that, even though the CoCrFeMnNi alloy has numerous excellent properties, as mentioned above, it decomposes to form an fcc phase and intermetallic phases such as a σ-phase when annealed at temperatures <800 °C [11–13]. These intermetallic phases are not desirable given than they have a negative influence on the ductility of alloys, even though their precipitation enhances the strength of an alloy [17]. It has been reported that, when the amount of those elements responsible for σ-phase formation, such as Cr and Mn, is high, the probability of its precipitation becomes very high [18]. As a result, these elements have been reported as being the source of the instability of the single fcc phase in a CoCrFeMnNi alloy [19]. An investigation into the phase stability of the non-equiatomic composition of the CoCrFeMnNi alloy system could be an ingenious way of exploring the possibility of σ-phase-free alloys by reducing the amounts of those elements responsible for its formation.

To predict the formation of a single-phase solid-solution alloy using the classic Hume–Rothery rules, several criteria have been proposed, such as the atomic size difference (δ), mixing enthalpy (ΔH_{mix}), mixing entropy (ΔS_{mix}), valence electron concentration (VEC), and electronegativity difference (Δχ) [20–23]. Previous studies have predicted that a random solid solution could be formed when the mixing enthalpies, mixing entropies, and atomic-size difference are within a range of -15–5 kJ/mol^{-1}, 12–17.5 J/K.mol^{-1}, and ≤4.3, respectively [24,25]. Guo et al. [20] proposed that the phase boundary between the bcc and fcc phases could be determined from the VEC; a sole fcc phase exists when VEC > 8, but the bcc phase exists only when VEC < 6.87. For example, for the equiatomic CoCrFeMnNi, VEC = 8 and $\Delta H_{mix} = -4.2$ kJ mol^{-1} [4,21]. This alloy has a single fcc phase except at temperatures <800 °C [12], correlating to the prediction of Guo et al. [20].

There have been several studies addressing the phase stability of a non-equiatomic composition of a CoCrFeMnNi alloy. Recently, Yao et al. [26] investigated the phase stability of non-equiatomic $Fe_{40}Co_5Cr_2Mn_{27}Ni_{26}$ and found that it contains a single fcc phase in spite of having a lower mixing entropy than the CoCrFeMnNi alloy. These results indicate that a careful adjustment of the equiatomic CoCrFeMnNi elements can lead to the formation of single-phase solid solutions in a HEA. Prior to the present work, there had been no studies addressing the effects of increasing the mole fraction of Fe in a CoCrFeMnNi system while maintaining the equiatomic composition of the other four elements. In the present study, a phase diagram for a CoCrMnNi-Fe system was proposed, which was followed up by an experimental investigation of $Fe_x(CoCrMnNi)_{100-x}$ alloys where $x = 00$, 20, 40, and 60 (atomic percent concentration). This alloy-design strategy offers the advantage of combining the desirable properties of a HEA and those of Fe-based high-alloy steels, such as high-Mn steel [27–30]. Additionally, it significantly reduces the cost of production by decreasing the required amounts of costly elements such as Co and Ni.

2. Material and methods

The alloy compositions in $Fe_x(CoCrMnNi)_{100-x}$ high- and medium-entropy systems were chosen by varying the amount of Fe from 0 to 60, hereafter referred to as Fe00, Fe20, Fe40, and Fe60, respectively. Cylindrical ingots (Ø15 mm × 120 mm) of the $Fe_x(CoCrMnNi)_{100-x}$ system were fabricated by arc melting and tilt-casting technique under a pure Ar atmosphere. Elements with purity >99.9% were used as the raw materials. The oxide layer on the Mn was removed with an aqueous solution of nitric acid, while the amount of Mn was adjusted to compensate for its high evaporation rate during the melting process. A Cu mold was used to cool the molten metal rapidly and to avoid Mn segregation during solidification. Phase identification was performed by X-ray diffraction (XRD, D8 Discover, Bruker) using Cu-Ka_1 radiation. The TCFE2000 thermodynamic database and its upgraded version [31,32] were used for the thermodynamic calculations [12,33]. Tensile tests were carried at room temperature using dog-bone-shaped specimens with a gauge length of 5 mm and a thickness of 1 mm with an initial strain rate of 8.3×10^{-4} s^{-1}. A digital image correlation technique was applied to precisely measure the strain. The specimens used for microstructure observation were prepared by first subjecting them to mechanical polishing and then electro-polishing using a solution of 10% perchloric acid and 90% acetic acid. Microstructure characterization was performed using a scanning electron microscope in electron-backscattered diffraction mode (SEM-EBSD).

3. Results

Fig. 1 shows the criterion used to select the chemical formulae of Fe00, Fe20, Fe40, Fe60, and Fe80 alloys. As mentioned above, all the specimens maintain a VEC of 8 but have different mixing enthalpies and entropies, as shown in Fig. 1. The mixing entropy of Fe00 is 11.53 J/K.mol^{-1}. The addition of 20 at.% Fe, to form an equiatomic CoCrFeMnNi alloy, increases the mixing entropy to 13.38 J/K.mol, which is the highest of any fabricated alloy. Further increasing the amount of Fe causes the mixing entropy to fall to zero for pure Fe, while the mixing enthalpy increases proportionally. Fe40 is also classified as a HEA whereas Fe00 and Fe60 are regarded as being MEAs, and Fe80 is a LEA [34]. As mentioned above, according to Zhang et al. [24], the mixing entropy range that warrants solid solution formation is 12–17.5 J/K.mol^{-1}. In the present work, the mixing entropies of Fe00, Fe20, and Fe40 fall within this range, but those of Fe60 (10.21 J/K.mol^{-1}) and Fe80 (6.45 J/K.mol) do not. However, the mixing enthalpies of all the alloys fall within the reported range [25]. Fig. 1b shows the change in the mixing enthalpy and the atomic size difference as a function of Fe. It can be deduced that increasing the Fe content reduces the atomic size difference while increasing the mixing entropy. All the alloys are within the solid solution region except for the Fe00 alloy, which is near the boundary separating the solid-solution and ordered-solid-solution regions. It should be noted that the Fe60 and Fe80 crystallize into fcc and bcc (not shown here) solid solutions, respectively, even though their mixing entropies fall slightly outside the reported range [25]. This indicates that the mixing entropy criterion probably cannot be used to determine the probability of solid solution formation at higher Fe contents. This is in good agreement with Yeh et al. [1], who stated that the effect of the entropy tends to be maximized in alloys with an equiatomic or near-equiatomic composition. Furthermore, the application of the VEC criterion is also limited to lower amounts of Fe since Fe80 crystallizes as a bcc phase, instead of the predicted fcc phase.

Fig. 2a shows the phase diagram of a CoCrMnNi-Fe system, which is somewhat different from that proposed by Bracq et al. [19] for low-temperature regimes. The diagram shows that a single-phase fcc structure can be obtained at 900 °C for Fe amounts much higher than 20%. These results prompted us to study the effects of Fe on the various physical properties of a non-equiatomic HEA or MEA system. Three important observations can be made from Fig. 2. First, the onset temperature of the σ phase found in

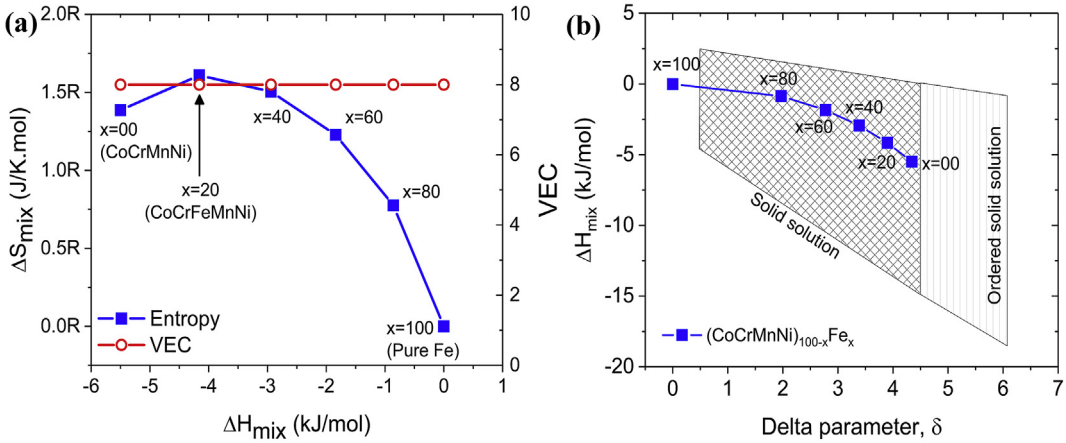

Fig. 1. Design strategy for the new fcc alloys for which VEC = 8. (a) Changes in ΔH_{mix} and ΔS_{mix} with different amounts of Fe in $Fe_x(CoCrMnNi)_{100-x}$ system ($x = 0$, 20, 40, 60, 80, and 100). R is the ideal gas constant (b) change in ΔH_{mix} and δ as a function of Fe.

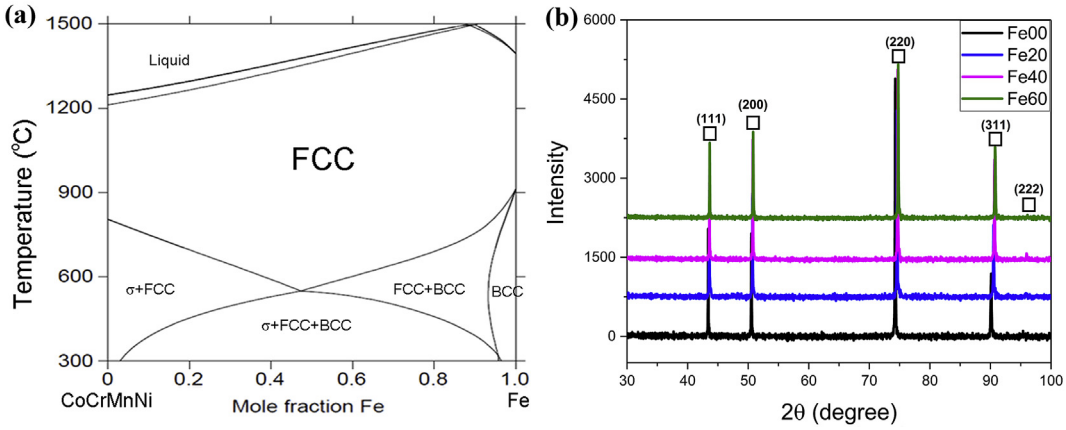

Fig. 2. (a) Phase diagram of CoCrMnNi-Fe system (b) XRD patterns of Fe00, Fe20, Fe40 and Fe60 annealed at 900 °C for 2 h.

Fe20 [11,12] decreases with an increase in the amount of Fe. Careful observation of the phase diagram reveals that the single fcc phase of Fe20 decomposes to form σ and fcc phases at temperatures <800 °C, which is consistent with the results of experiments reported in the literature [11,12]. Second, the single fcc phase can exist even at low temperatures of approximately 600 °C in an Fe50 system. Finally, the melting temperature decreases with the Fe content in both the HEA and MEA regimes. The XRD patterns of the Fe00, Fe20, Fe40, and Fe60 specimens annealed at 900 °C for 2 h are presented in Fig. 2b. Note that all the alloys exhibit a single fcc phase, which is consistent with the thermodynamic calculation presented in Fig. 2a.

Fig. 3a shows the engineering stress-strain curves of Fe00, Fe20, Fe40, and Fe60. With an increase in the Fe content, both the yield strength (YS) and ultimate tensile strength (UTS) decrease, but the uniform elongation (UE) increases. The change in UTS and UE as the Fe content is increased from 0 to 100, is presented in Fig. 3b. The UTS of Fe00 is exceptionally high compared to that of the other alloys but its UE is reduced to 18%. The decrement of the UTS occurs in two stages: The first stage is a significant decrease from 810 MPa for Fe00 to 610 MPa for Fe20, which indicates that the introduction of 20 at.% Fe results in a 200 MPa decrease in the strength. In the second stage, there is a gradual decrease in the UTS from 610 MPa for Fe20 to 560 MPa for Fe60. The change in the UTS when the amount of Fe is increased from Fe20 to Fe60 is relatively insignificant. The difference in the UTS values of Fe20 and Fe40 is 25 MPa, while that between Fe40 and Fe60 is 20 MPa. On the other hand, increasing the Fe content in consistent increments of 20 at.% produces a variable change in the UE. At Fe20, a UE increase of 8% is observed, which is similar to the 9% increase observed for Fe40. The greatest change in the UE, of 15%, is observed for Fe60. This exceptional increase in the UE, especially after increasing the Fe content to 60 at.%, may be an indication of an additional deformation mechanism, such as deformation twinning, which is known to enhance the mechanical properties of metals and alloys [35–37].

Fig. 4 shows the inverse pole figure (IPF) maps of the tensile-tested specimens, which are interrupted at different true strains. The IPF maps for (a) Fe00, (d, e) Fe20, (h, i) Fe40, and (l, m) Fe60 were obtained from specimens deformed up to different true strain levels, which is referred to as ε_T in the present work. On the other hand, the IPF maps for (b) Fe00, (f) Fe20, (j) Fe40, and (n) Fe60 were obtained from the necking area and, therefore, their strain is referred to as a local strain (denoted as ε_L). Note that the ε_L values presented in Fig. 4 exceed the true strain values due to the localized deformation in the necking area during tensile testing. As mentioned above, the DIC technique was used to precisely measure the local strain. Images showing the localized strain in the necking area are presented in Fig. 4 (c, g, k, and o).

The IPF maps showing texture evolution during tensile test are presented in Fig. 4. At lower true strains, i.e., 8%, a random texture

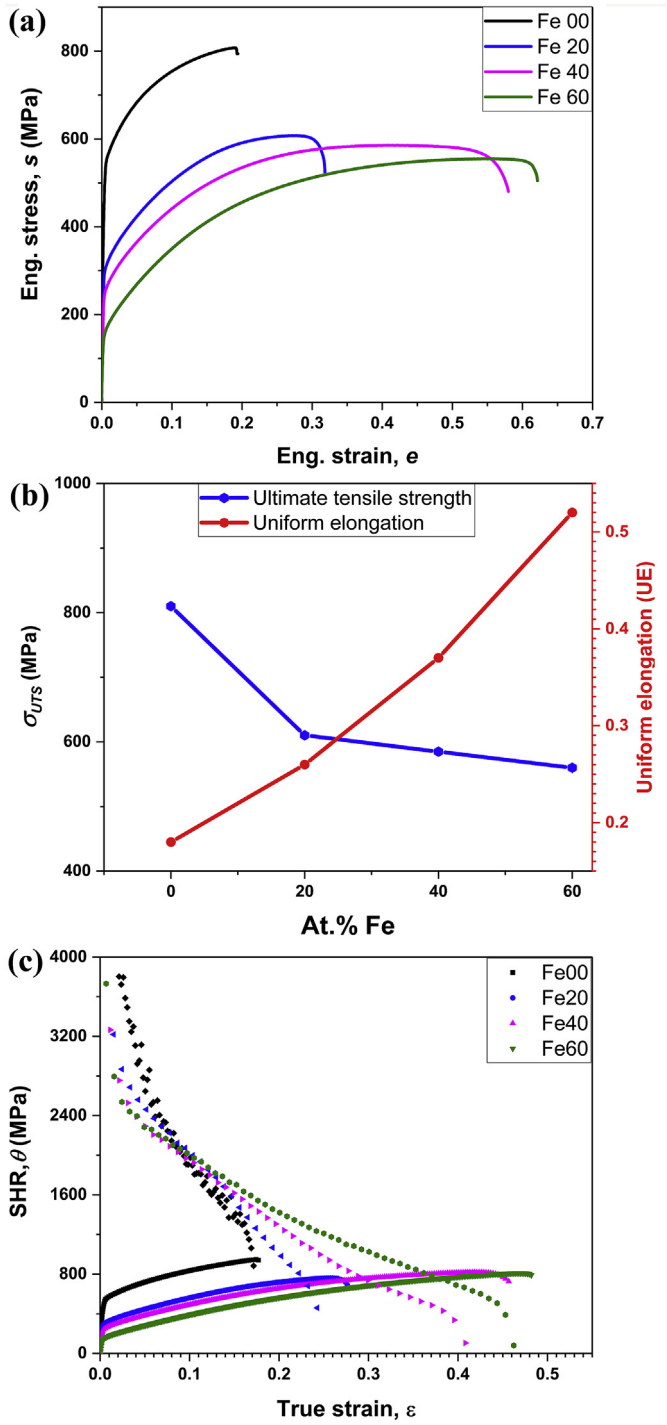

Fig. 3. (a) Engineering stress-strain curve, (b) yield strength, ultimate tensile strength, and uniform elongation as a function of at.% Fe, and (c) strain hardening behavior of Fe00, Fe20, Fe40 and Fe60.

with components <111>//TD, <101>//TD, and <001>//TD (where TD is the tensile direction) is observed, especially in Fe00, Fe20, and Fe40 as shown in Fig. 4 (a, d, and h). However, at the same strain, Fe60 shows strong <111>//TD and <001>//TD texture components, as shown in Fig. 4m. The IPF maps from the necking area indicate that the <111>//TD and <001>//TD texture components are preferred to the <101>//TD texture component, as shown in Fig. 4 (b, f, j, and n). This phenomenon is similar to that of typical fcc metals and alloys [18]. This tendency remains constant regardless of the Fe content.

A Fe00 alloy exhibits a inhomogeneous microstructure with a high area fraction of ultra-fine grains (UFG), even though the annealing conditions are similar to those of other alloys. The UFG microstructure in Fe00 has a grain size of approximately 0.6 μm, while the size of the coarse grains is approximately 6 μm Fe20 to Fe60 contain an equiaxed microstructure with a mean grain size of 8 μm. The Fe00 contains no deformation twins (DTs) in those specimens strained up to 8% of the true strain and true stress of 792 MPa, but a small number is observed in the necking area specimen with a local strain of 28%. They are mostly observed in the few coarse grains and not in the UFG. The Fe20 specimens that are interrupted at 8% and 15% true strains with corresponding true stresses of 517 MPa and 654 MPa, respectively, show no DT. Moreover, numerous DT are observed in the necking area of the Fe20. The Fe40 specimens deformed up to 8% and 20% of the true strain with corresponding true stresses of 450 MPa and 657 MPa, respectively, also exhibit no DT. In addition, the Fe40 exhibits large amounts of DT in the necking-area specimen (Fig. 4j). Nevertheless, one notable difference between the specimen obtained from the necking area of Fe40 and that taken from the necking area of Fe20 is the frequency and the width of the DT. The DT frequency is higher in Fe40, while the widths are larger than those in Fe20. The tendency of the absence of DT also extends to the Fe60 specimen that is deformed up to 8% of the true strain and a corresponding true stress of 348 MPa. Nevertheless, it is interesting to note that DTs are observed in the specimen that is strained up to 20% of the true strain with a true stress component of 563 MPa, as shown in Fig. 4m. Furthermore, the DT frequency in the necking area of Fe60, as shown in Fig. 4n, is higher than those in the necking areas of the Fe20 and Fe40 specimens. Most grains with DT possess multiple twinning systems, sometimes up to three per grain. Similar multiple twinning systems have been reported for twin-induced plasticity (TWIP) steel [28]. The DT for a sample strained up to 20% can be clearly distinguished from the annealing twins since the latter occur randomly irrespective of the orientation of the grains. On the other hand, DTs predominantly form on those grains oriented in the <111> direction [38].

Fig. 5 shows the evolution of the DT frequency as a function of at.% Fe. To evaluate the effect of increasing the amount of Fe on the evolution of DTs, those specimens exhibiting massive twinning, as shown in Fig. 4 (b, f, j, and n), were used. A simple technique was adopted to evaluate the frequency of deformation in each alloy. Five equally spaced lines were drawn on each IPF map, and the number of DTs ($\sum 3$ boundary) intersecting those lines was summed. The standard deviation of each data point was also included. It was found that Fe00 has the lowest DT frequency in its microstructure while Fe60 has the highest one.

4. Discussion

Fig. 3c shows the strain hardening rate (SHR) curves for Fe00 to Fe60. Generally, the four SHR curves exhibit two distinct stages. The first stage is characterized by an almost zero strain hardening, wherein the SHR decreases constantly. The second stage consists of a monotonic decrease in the SHR up to the necking point. It was observed that the strain in the second stage increases as the amount of Fe is increased. Moreover, Fe20, Fe40, and Fe60 exhibit post-elongation, while the Fe00 fractures immediately after exhibiting plastic instability. Additionally, it can be seen that an increase in the amount of Fe shifts the SHR curve upwards. The plastic instability, which occurs when $\theta < \sigma_T$ as stated in the Considère criterion [39], is postponed further as the Fe content is

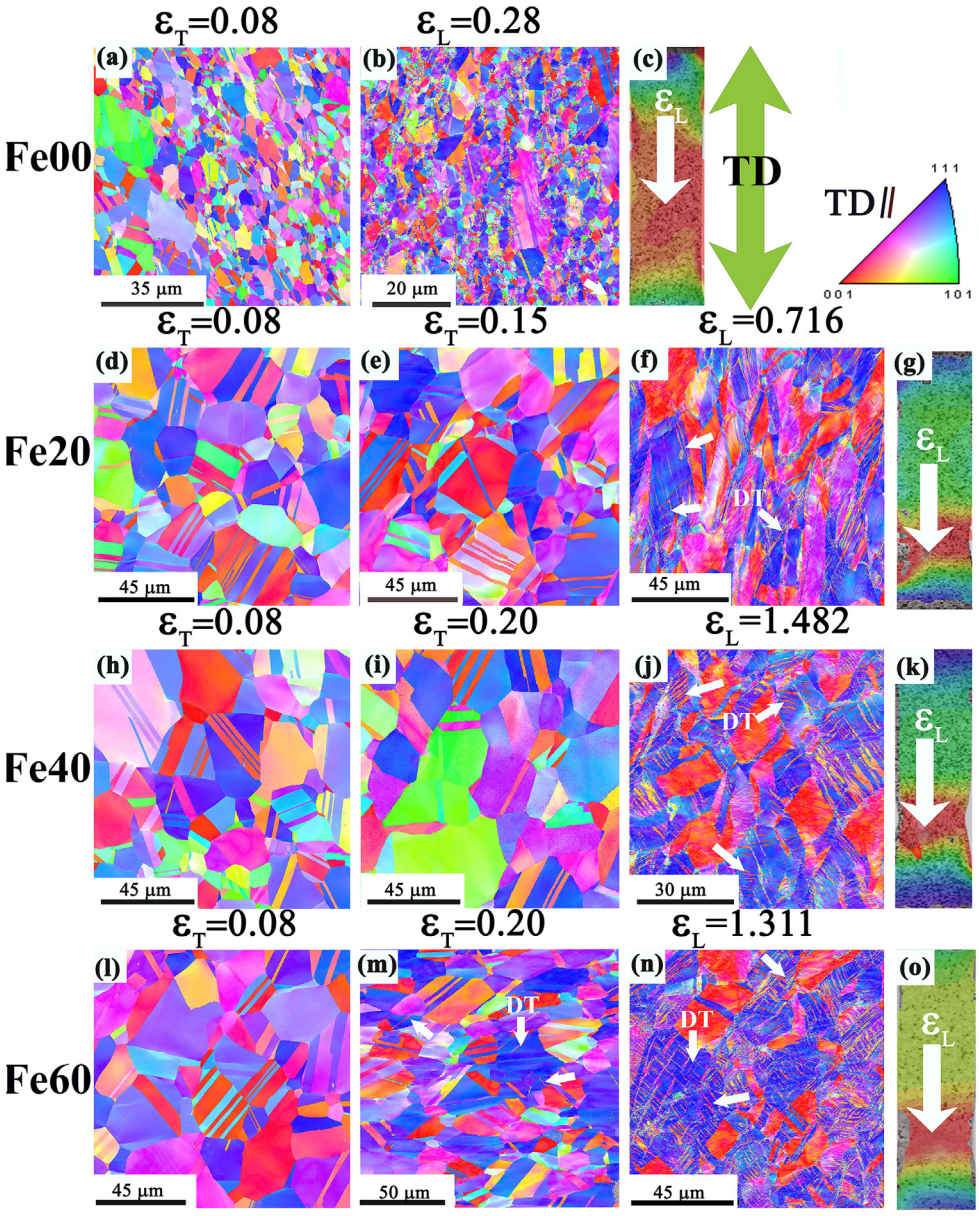

Fig. 4. EBSD inverse pole figure (IPF) maps of tensile-tested specimens at different strains. Fe00 (a = 8%), Fe20 (d = 8%, e = 15%), Fe40 (h = 8%, i = 20%) and Fe60 (l = 8%, m = 20%) are deformed to various true strain values, referred to as ε_T. Fe00 (b = 28%), Fe20 (f = 72%), Fe40 (j = 148%), and Fe60 (n = 131%) are obtained from the necking area and, therefore, their strains are referred to as local strains (ε_L). c, g, k, and o are DIC images showing the localized strain in the necking area. DT is the deformation twin and TD is the tensile direction.

increased ($\theta = d\sigma_T/d\varepsilon_T$ where σ_T and ε_T are the true stress and true strain, respectively). The postponement of the plastic instability at higher Fe contents could be due to the additional deformation mechanism, such as deformation twinning, wherein the twin boundaries act as obstacles to the dislocation motion and, therefore, increase the UTS of metals and alloys [14,37]. Recent studies have found that deformation twinning is easily instigated in low stacking fault energy (SFE) metals and alloys [14,28,40]. Therefore, an increase in the Fe content in the present study probably results in a significant decrease in the SFE, which in turn leads to the formation of DTs, leading to an upward shift in the SHR and the postponement of the plastic instability.

The UFG of the Fe00 is one of the factors responsible for its high YS and UTS, but minimal UE, relative to other alloys, as shown in Fig. 3a [41]. As previously mentioned, the probability of σ phase formation is inevitably high, especially when there are large amounts of elements such as Cr and Mn, which are responsible for its formation [18]. An Fe00 alloy contains 25 at.% each of these elements and, therefore, increases the probability of σ phase formation [18]. The high volume fraction of UFG in Fe00, even after high-temperature annealing, could be a result of grain growth inhibition by second phases such as the σ phase. Additionally, the presence of a small fraction of coarse grains indicates the possibility of abnormal grain growth, as shown in Fig. 4a. According to Dennis et al. [42], the pinning effect of the second phases can result in abnormal grain growth which, to some extent, may lead to poor mechanical properties. The above phenomena could be an additional reason for the high strength, but decreased ductility exhibited by an Fe00 alloy. Moreover, even though the precipitation of the σ phase in the phase diagram shown in Fig. 2a is < 900 °C, that is, the annealing temperature used in the present work, there is a possibility of it forming at or above this temperature for Fe00.

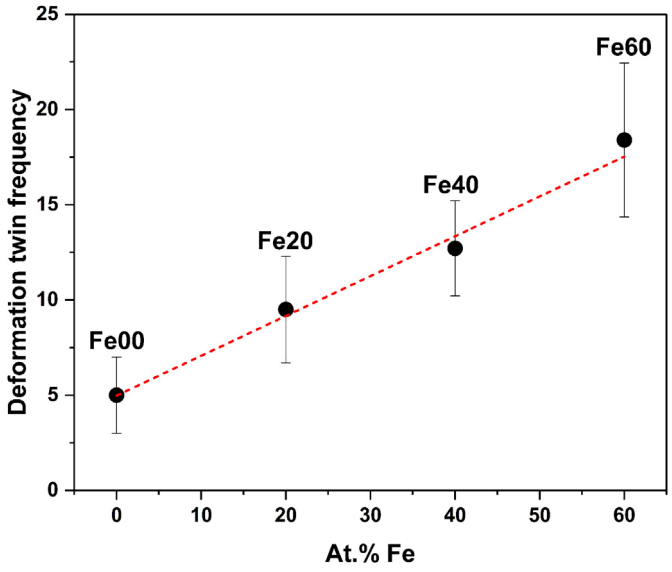

Fig. 5. Evolution of deformation twin frequency as a function of at.% Fe measured from the specimens obtained prior to fracture. The red line (short dashes) is the linear fitting of the data. (For interpretation of the references to colour in this figure legend, the reader is referred to the Web version of this article.)

To the best of our knowledge, there have been no reports addressing an Fe00 alloy system. Therefore, further microstructural characterization is required to validate our hypothesis about the presence of the second phases.

Recent studies have reported that dislocation glide is the dominant deformation mechanism in HEAs at lower strain regimes when deformed at room temperature [14,37,43]. On the other hand, deformation twinning is reported to be an additional deformation mechanism at higher strains in HEAs [36,44]. Otto et al. [14] studied the deformation mechanism of CoCrFeMnNi under both cryogenic and room-temperature conditions. They concluded that deformation twinning occurs only under cryogenic conditions and not at room temperature. Nonetheless, Laplanche et al. [43], unlike Otto et al. [14], proposed that deformation twinning did not occur at room temperature in the latter work, probably because the specimens were not sufficiently deformed. To validate this hypothesis, Laplanche et al. [43], conducted a study of the evolution of the microstructure of a CoCrFeMnNi HEA with a specific emphasis on the onset of deformation twinning. They found that twinning occurs at true strains >20%. They concluded that the critical twinning stress is 720 ± 30 MPa.

In the present study, a similar approach was employed to investigate the evolution of the microstructure of each alloy at various true strains, while monitoring the onset of twinning. DTs were not observed in Fe00 at a true strain of 8% with a corresponding true stress of ca. 790 MPa. Even though this true stress value is greater than the critical twinning stress mentioned in Ref. [43], deformation twinning is not easily detected. This could be due to the high volume fraction of UFG present in this specimen. Sun et al. [45] studied the effect of grain refinement on the twinning behavior of a CoCrFeMnNi HEA. They observed that deformation twinning occurs easily in a coarse-grain regime; however, it is significantly suppressed in a UFG regime due to the increased critical twinning stress. The inability to detect the DT at a true strain of 8% for Fe00 is probably due to the low magnification of the EBSD, relative to the TEM used in other studies [43,45]. A careful examination of the specimen taken from the necking area, which corresponds to a true stress of approximately 950 MPa, reveals some DT, especially in those grains with an orientation parallel to the <111> direction, which is favorable for deformation twinning [38]. This stress could be sufficiently high to instigate DT, even though they are not present in sufficient numbers to have a noticeable effect on the mechanical properties of Fe00. In those Fe20 specimens deformed to 8% and 15%, DTs are not observed because their true stress components of 517 MPa and 654 MPa, respectively, are below the critical twinning stress [43]. Additionally, the high true stress of 761 MPa leads to considerable DT in the necking area specimen of Fe20. A similar phenomenon is observed in Fe40, for which no DT is observed in those specimens strained up to 8% and 20% due to their low true stresses, both of which are below the critical twinning stress. A high true stress of 820 MPa in the necking region (Fig. 4j), causes considerable DT. Unlike in the other alloys, the DTs are activated in Fe60 at a lower strain of 20% and a true stress of 563 MPa. This value is lower than the 720 ± 30 MPa that was obtained by Laplanche et al. [43] for Fe20. Therefore, it can be concluded that the addition of Fe lowers the critical twinning stress. The grain size [46] is a parameter that significantly affects the critical twinning stress and, therefore, it is imperative that its effect be considered in the present study. The grain size in the present work was maintained at a relatively constant value of approximately 8 μm for all the alloys other than Fe00. Therefore, this value is less than half the 17 μm reported by Laplanche et al. [43]. Therefore, the reported critical twinning stress for Fe60 (563 MPa) could be reduced even further if a coarser grain size were to be used (for example, 17 μm). Consequently, using a microstructure with such a grain size (17 μm) may result in DT being instigated at a lower true strain in Fe40, which does not have DT, even for 20% of the true strain deformation.

It can be deduced that the DT frequency increases proportionally due to the increase in the Fe content, as shown in Fig. 5. The deformation twinning mechanism has been reported as significantly enhancing the mechanical properties by acting as a barrier to dislocation motion, hence postponing the plastic instability. Therefore, it has attracted considerable attention, especially in the area of TWIP steels [47] and, more recently, of HEAs [48,49]. The formation of DTs has been reported as being a function of the grain size [46], temperature [50], strain rate, and SFE [51]. All these factors, other than SFE, were kept constant at ca. 8 μm, room temperature, and 8.3×10^{-4} $s^{-1,}$ respectively, for Fe00 to Fe60. Therefore, the deformation twinning mechanism observed in the present study is probably controlled by SFE, given that they possess compositional variance. It has been reported that, depending on a particular SFE regime, metals and alloys exhibit different deformation mechanisms. When SFE is >ca. 45 mJ/m^2, dislocation slip is the dominant deformation mechanism, between 18 and 45 mJ/m^2, metals and alloys deform as a result of a combination of dislocation glide and deformation twinning. When the SFE is < 18 mJ/m^2 dislocation glide and martensitic transformation are the dominant deformation mechanisms [52,53] The present study revealed that increasing the amount of Fe decreases the critical twinning stress but the DT frequency increases proportionally. Therefore, it is reasonable to assume that, for higher Fe amounts, the SFE becomes lower such that DT is easily instigated. It is possible that increasing the amount of Fe to >60 at.% would result in a further reduction in the SFE, which would trigger the transformation-induced plasticity (TRIP) during the deformation. Stainless steels, such as SS 304 and SS 316 (which are also classified as MEAs or LEAs), have been reported as exhibiting the TRIP phenomenon [54,55]. Consequently, the similarity in the deformation mechanisms of HEA and stainless steel, provides a platform for the design of new metallic alloys that combine the advantageous properties of HEAs and high-alloyed steels. Nonetheless, to fully confirm this hypothesis, further studies are required to elucidate the SFE evolution as a function of

the Fe content. Also, experimental investigations of alloys with Fe contents >60 at.% will be necessary to reveal the deformation mechanism.

5. Conclusions

In the present study, Fe00, Fe20, Fe40, and Fe60 alloys with a constant VEC of 8 were successfully fabricated, bridging the gap between HEAs and stainless steels. Based on the experimental results, the following conclusions can be drawn:

1. A phase diagram of CoCrMnNi-Fe system was presented. According to this phase diagram, increasing the Fe content reduces the melting temperature and the onset temperature of the undesirable σ phase, with Fe50 having a single phase fcc, even at 600 °C. The alloys exhibit a single-phase fcc structure after annealing at 900 °C. Additionally, the probability of the formation of a bcc phase increases with the increase in the Fe content. Our experimental results confirmed that Fe20, Fe40, and F60 have a single-phase fcc, which is in good agreement with the results of the thermodynamic calculations.
2. While YS and UTS decrease, UE increases as the Fe content is increased. Additionally, the strain-hardening rate is significantly enhanced at higher Fe contents for which the postponement of the plastic instability is observed. This is attributed to the instigation of DT, acting as an additional deformation mechanism in alloys with a higher Fe content, as in the case of Fe60.
3. The critical twinning stress is significantly reduced at higher Fe contents. The Fe60 specimen, which was deformed up to 20% of the true strain with a true stress of 563 MPa, exhibited the formation of DTs, unlike the other alloys. This value is less than that of the Fe20 reported in the literature. The DT frequency is also higher in Fe60, compared to the other alloys, due to the reduced critical twinning stress.

Acknowledgement

This study has been supported by the National Research Foundation of Korea funded by the Korean government (Ministry of Science, ICT and Future Planning, MSIP) (NRF-2016M3D1A1023384 (Future Material Discovery Program)).

References

[1] J.W. Yeh, S.K. Chen, S.J. Lin, J.Y. Gan, T.S. Chin, T.T. Shun, C.H. Tsau, S.Y. Chang, Nanostructured high-entropy alloys with multiple principal elements: novel alloy design concepts and outcomes, Adv. Eng. Mater. (2004), https://doi.org/10.1002/adem.200300567.
[2] M. Feuerbacher, T. Lienig, C. Thomas, A single-phase bcc high-entropy alloy in the refractory Zr-Nb-Ti-V-Hf system, Scripta Mater. (2018), https://doi.org/10.1016/j.scriptamat.2018.04.009.
[3] M.-H. Tsai, J.-W. Yeh, High-entropy alloys: a critical review, Mater. Res. Lett. 2 (2014) 107–123, https://doi.org/10.1080/21663831.2014.912690.
[4] B. Cantor, I.T.H. Chang, P. Knight, A.J.B. Vincent, Microstructural development in equiatomic multicomponent alloys, Mater. Sci. Eng. A 375–377 (2004) 213–218, https://doi.org/10.1016/j.msea.2003.10.257.
[5] A. Takeuchi, K. Amiya, T. Wada, K. Yubuta, W. Zhang, High-entropy alloys with a hexagonal close-packed structure designed by equi-atomic alloy strategy and binary phase diagrams, JOM 66 (2014) 1984–1992, https://doi.org/10.1007/s11837-014-1085-x.
[6] B. Gludovatz, A. Hohenwarter, D. Catoor, E.H. Chang, E.P. George, R.O. Ritchie, A fracture-resistant high-entropy alloy for cryogenic applications, Science 345 (2014) 1153–1158, https://doi.org/10.1126/science.1254581.
[7] K.T. Park, K.G. Jin, S.H. Han, S.W. Hwang, K. Choi, C.S. Lee, Stacking fault energy and plastic deformation of fully austenitic high manganese steels: effect of Al addition, Mater. Sci. Eng. A (2010), https://doi.org/10.1016/j.msea.2010.02.058.
[8] R. Pederson, F. Niklasson, F. Skystedt, R. Warren, Microstructure and mechanical properties of friction- and electron-beam welded Ti-6Al-4V and Ti-6Al-2Sn-4Zr-6Mo, Mater. Sci. Eng. A (2012), https://doi.org/10.1016/j.msea.2012.05.087.
[9] J.W. Yeh, Physical metallurgy of high-entropy alloys, JOM 67 (2015) 2254–2261, https://doi.org/10.1007/s11837-015-1583-5.
[10] E.J. Pickering, R. Muñoz-Moreno, H.J. Stone, N.G. Jones, Precipitation in the equiatomic high-entropy alloy CrMnFeCoNi, Scripta Mater. 113 (2016), https://doi.org/10.1016/j.scriptamat.2015.10.025.
[11] B. Schuh, F. Mendez-Martin, B. Volker, E.P. George, H. Clemens, R. Pippan, A. Hohenwarter, Mechanical properties, microstructure and thermal stability of a nanocrystalline CoCrFeMnNi high-entropy alloy after severe plastic deformation, Acta Mater. 96 (2015) 258–268, https://doi.org/10.1016/j.actamat.2015.06.025.
[12] N. Park, B.J. Lee, N. Tsuji, The phase stability of equiatomic CoCrFeMnNi high-entropy alloy: comparison between experiment and calculation results, J. Alloy. Comp. 719 (2017) 189–193, https://doi.org/10.1016/j.jallcom.2017.05.175.
[13] F. Otto, A. Dlouhý, K.G. Pradeep, M. Kuběnová, D. Raabe, G. Eggeler, E.P. George, Decomposition of the single-phase high-entropy alloy CrMnFeCoNi after prolonged anneals at intermediate temperatures, Acta Mater. (2016), https://doi.org/10.1016/j.actamat.2016.04.005.
[14] F. Otto, A. Dlouhý, C. Somsen, H. Bei, G. Eggeler, E.P. George, The influences of temperature and microstructure on the tensile properties of a CoCrFeMnNi high-entropy alloy, Acta Mater. 61 (2013) 5743–5755, https://doi.org/10.1016/j.actamat.2013.06.018.
[15] W.H. Liu, Y. Wu, J.Y. He, T.G. Nieh, Z.P. Lu, Grain growth and the Hall-Petch relationship in a high-entropy FeCrNiCoMn alloy, Scripta Mater. 68 (2013) 526–529, https://doi.org/10.1016/j.scriptamat.2012.12.002.
[16] F. Dobeš, H. Hadraba, Z. Chlup, A. Dlouhý, M. Vilémová, J. Matějíček, Compressive creep behavior of an oxide-dispersion-strengthened CoCrFeMnNi high-entropy alloy, Mater. Sci. Eng. A 732 (2018) 99–104, https://doi.org/10.1016/j.msea.2018.06.108.
[17] J. Lee, I. Kim, A. Kimura, Application of small punch test to evaluate sigma-phase embrittlement of pressure vessel cladding material, J. Nucl. Sci. Technol. (2003), https://doi.org/10.1080/18811248.2003.9715404.
[18] C.-C. Hsieh, W. Wu, Overview of intermetallic sigma ( ) phase precipitation in stainless steels, ISRN Metall. 2012 (2012) 1–16, https://doi.org/10.5402/2012/732471.
[19] G. Bracq, M. Laurent-Brocq, L. Perrière, R. Pirès, J.-M. Joubert, I. Guillot, The fcc solid solution stability in the Co-Cr-Fe-Mn-Ni multi-component system, Acta Mater. 128 (2017) 327–336, https://doi.org/10.1016/j.actamat.2017.02.017.
[20] S. Guo, C. Ng, J. Lu, C.T. Liu, Effect of valence electron concentration on stability of fcc or bcc phase in high entropy alloys, J. Appl. Phys. 109 (2011) 103505, https://doi.org/10.1063/1.3587228.
[21] Y. Zhang, T.T. Zuo, Z. Tang, M.C. Gao, K.A. Dahmen, P.K. Liaw, Z.P. Lu, Microstructures and properties of high-entropy alloys, Prog. Mater. Sci. 61 (2014) 1–93, https://doi.org/10.1016/j.pmatsci.2013.10.001.
[22] Z.D. Sha, L.C. He, S. Xu, Q.X. Pei, Z.S. Liu, Y.W. Zhang, T.J. Wang, Effect of aspect ratio on the mechanical properties of metallic glasses, Scripta Mater. 93 (2014) 36–39, https://doi.org/10.1016/j.scriptamat.2014.08.025.
[23] A. Takeuchi, A. Inoue, Classification of bulk metallic glasses by atomic size difference, heat of mixing and period of constituent elements and its application to characterization of the main alloying element, Mater. Trans. 46 (2005) 2817–2829, https://doi.org/10.2320/matertrans.46.2817.
[24] Y. Zhang, Y.J. Zhou, J.P. Lin, G.L. Chen, P.K. Liaw, Solid-solution phase formation rules for multi-component alloys, Adv. Eng. Mater. 10 (2008) 534–538, https://doi.org/10.1002/adem.200700240.
[25] Z. Wang, S. Guo, C.T. Liu, Phase selection in high-entropy alloys: from nonequilibrium to equilibrium, JOM 66 (2014) 1966–1972, https://doi.org/10.1007/s11837-014-0953-8.
[26] M.J. Yao, K.G. Pradeep, C.C. Tasan, D. Raabe, A novel, single phase, non-equiatomic FeMnNiCoCr high-entropy alloy with exceptional phase stability and tensile ductility, Scripta Mater. 72–73 (2014) 5–8, https://doi.org/10.1016/j.scriptamat.2013.09.030.
[27] H. Idrissi, L. Ryelandt, M. Veron, D. Schryvers, P.J. Jacques, Is there a relationship between the stacking fault character and the activated mode of plasticity of Fe-Mn-based austenitic steels? Scripta Mater. 60 (2009) 941–944, https://doi.org/10.1016/j.scriptamat.2009.01.040.
[28] I. Gutierrez-Urrutia, D. Raabe, Dislocation and twin substructure evolution during strain hardening of an Fe-22 wt.% Mn-0.6 wt.% C TWIP steel observed by electron channeling contrast imaging, Acta Mater. (2011), https://doi.org/10.1016/j.actamat.2011.07.009.
[29] O. Grässel, L. Krüger, G. Frommeyer, L.W. Meyer, High strength Fe-Mn-(Al, Si) TRIP/TWIP steels development - properties - application, Int. J. Plast. (2000), https://doi.org/10.1016/S0749-6419(00)00015-2.
[30] O. Grässel, L. Krüger, G. Frommeyer, L. Meyer, High strength Fe–Mn–(Al, Si) TRIP/TWIP steels development — properties — application, Int. J. Plast. 16 (2000) 1391–1409, https://doi.org/10.1016/S0749-6419(00)00015-2.
[31] TCFE2000, The Thermo-Calc Steels Database, Upgraded by B.-J. Lee, B. Sundman at KTH, KTH, Stockholm, 1999 (n.d.).
[32] K.G. Chin, H.J. Lee, J.H. Kwak, J.Y. Kang, B.J. Lee, Thermodynamic calculation on the stability of (Fe,Mn)3AlC carbide in high aluminum steels, J. Alloy. Comp. 505 (2010) 217–223, https://doi.org/10.1016/j.jallcom.2010.06.032.
[33] W.-M. Choi, S. Jung, Y.H. Jo, S. Lee, B.-J. Lee, Design of new face-centered cubic high entropy alloys by thermodynamic calculation, Met. Mater. Int. 23 (2017) 839–847, https://doi.org/10.1007/s12540-017-6701-1.
[34] J.-W. Yeh, Alloy design strategies and future trends in high-entropy alloys, JOM 65 (2013) 1759–1771, https://doi.org/10.1007/s11837-013-0761-6.

[35] Y. Wang, B. Liu, K. Yan, M. Wang, S. Kabra, Y.L. Chiu, D. Dye, P.D. Lee, Y. Liu, B. Cai, Probing deformation mechanisms of a FeCoCrNi high-entropy alloy at 293 and 77 K using in situ neutron diffraction, Acta Mater. (2018), https://doi.org/10.1016/j.actamat.2018.05.013.
[36] B. Wang, H. He, M. Naeem, S. Lan, S. Harjo, T. Kawasaki, Y. Nie, H.W. Kui, T. Ungár, D. Ma, A.D. Stoica, Q. Li, Y. Ke, C.T. Liu, X.-L. Wang, Deformation of CoCrFeNi high entropy alloy at large strain, Scripta Mater. 155 (2018) 54–57, https://doi.org/10.1016/j.scriptamat.2018.06.013.
[37] G. Laplanche, A. Kostka, C. Reinhart, J. Hunfeld, G. Eggeler, E.P. George, Reasons for the superior mechanical properties of medium-entropy CrCoNi compared to high-entropy CrMnFeCoNi, Acta Mater. (2017), https://doi.org/10.1016/j.actamat.2017.02.036.
[38] D. Barbier, N. Gey, S. Allain, N. Bozzolo, M. Humbert, Analysis of the tensile behavior of a TWIP steel based on the texture and microstructure evolutions, Mater. Sci. Eng. A (2009), https://doi.org/10.1016/j.msea.2008.09.031.
[39] R.E. Smallman, R.J. Bishop, Mechanical behaviour of materials, in: Mod. Phys. Metall. Mater. Eng, Elsevier, 1999, pp. 197–258, https://doi.org/10.1016/B978-075064564-5/50007-0.
[40] Y.Z. Tian, Y. Bai, L.J. Zhao, S. Gao, H.K. Yang, A. Shibata, Z.F. Zhang, N. Tsuji, A novel ultrafine-grained Fe–22Mn–0.6C TWIP steel with superior strength and ductility, Mater. Char. 126 (2017) 74–80, https://doi.org/10.1016/j.matchar.2016.12.026.
[41] M. El-Tahawy, P.H.R. Pereira, Y. Huang, H. Park, H. Choe, T.G. Langdon, J. Gubicza, Exceptionally high strength and good ductility in an ultrafine-grained 316L steel processed by severe plastic deformation and subsequent annealing, Mater. Lett. 214 (2018) 240–242, https://doi.org/10.1016/j.matlet.2017.12.040.
[42] J. Dennis, P.S. Bate, F.J. Humphreys, Abnormal grain growth in Al–3.5Cu, Acta Mater. (2009), https://doi.org/10.1016/j.actamat.2009.06.018.
[43] G. Laplanche, A. Kostka, O.M. Horst, G. Eggeler, E.P. George, Microstructure evolution and critical stress for twinning in the CrMnFeCoNi high-entropy alloy, Acta Mater. (2016), https://doi.org/10.1016/j.actamat.2016.07.038.
[44] W.H. Liu, Z.P. Lu, J.Y. He, J.H. Luan, Z.J. Wang, B. Liu, Y. Liu, M.W. Chen, C.T. Liu, Ductile CoCrFeNiMo x high entropy alloys strengthened by hard intermetallic phases, Acta Mater. 116 (2016) 332–342, https://doi.org/10.1016/j.actamat.2016.06.063.
[45] S.J. Sun, Y.Z. Tian, H.R. Lin, H.J. Yang, X.G. Dong, Y.H. Wang, Z.F. Zhang, Transition of twinning behavior in CoCrFeMnNi high entropy alloy with grain refinement, Mater. Sci. Eng. A 712 (2018) 603–607, https://doi.org/10.1016/j.msea.2017.12.022.
[46] Y.T. Zhu, X.Z. Liao, X.L. Wu, J. Narayan, Grain size effect on deformation twinning and detwinning, J. Mater. Sci. 48 (2013) 4467–4475, https://doi.org/10.1007/s10853-013-7140-0.
[47] I. Gutierrez-Urrutia, S. Zaefferer, D. Raabe, Electron channeling contrast imaging of twins and dislocations in twinning-induced plasticity steels under controlled diffraction conditions in a scanning electron microscope, Scripta Mater. (2009), https://doi.org/10.1016/j.scriptamat.2009.06.018.
[48] Y.H. Jo, S. Jung, W.M. Choi, S.S. Sohn, H.S. Kim, B.J. Lee, N.J. Kim, S. Lee, Cryogenic strength improvement by utilizing room-temperature deformation twinning in a partially recrystallized VCrMnFeCoNi high-entropy alloy, Nat. Commun. (2017), https://doi.org/10.1038/ncomms15719.
[49] Z. Wu, C.M. Parish, H. Bei, Nano-twin mediated plasticity in carbon-containing FeNiCoCrMn high entropy alloys, J. Alloy. Comp. (2015), https://doi.org/10.1016/j.jallcom.2015.05.224.
[50] M.A. Meyers, O. Vöhringer, V.A. Lubarda, The onset of twinning in metals: a constitutive description, Acta Mater. (2001), https://doi.org/10.1016/S1359-6454(01)00300-7.
[51] S. Curtze, V.T. Kuokkala, Dependence of tensile deformation behavior of TWIP steels on stacking fault energy, temperature and strain rate, Acta Mater. (2010), https://doi.org/10.1016/j.actamat.2010.05.049.
[52] S. Allain, J.-P. Chateau, O. Bouaziz, A physical model of the twinning-induced plasticity effect in a high manganese austenitic steel, Mater. Sci. Eng. A 387–389 (2004) 143–147, https://doi.org/10.1016/j.msea.2004.01.060.
[53] G.B. Olson, M. Cohen, A mechanism for the strain-induced nucleation of martensitic transformations, J. Less Common Met. 28 (1972) 107–118, https://doi.org/10.1016/0022-5088(72)90173-7.
[54] N. Solomon, I. Solomon, Deformation induced martensite in AISI 316 stainless steel, Rev. Metal. (2010), https://doi.org/10.3989/revmetalm.0920.
[55] Z. Tourki, H. Bargui, H. Sidhom, The kinetic of induced martensitic formation and its effect on forming limit curves in the AISI 304 stainless steel, J. Mater. Process. Technol. (2005), https://doi.org/10.1016/j.jmatprotec.2003.08.010.